AIAA JOURNAL
Vol. 49, No. 2, February 2011

Improvement of Axial Buckling Capacity of Elliptical Lattice Cylinders

Maurizio Paschero*
University of Rome "La Sapienza," 00184 Rome, Italy
and
Michael W. Hyer†
Virginia Polytechnic Institute and State University, Blacksburg, Virginia 24061

DOI: 10.2514/1.J050725

A formulation to improve the axial buckling capacity of elliptical lattice cylinders by varying the lattice rib angle as a function of circumferential location is discussed. The isogrid lattice is a classic case, and a circular cylinder with an isogrid construction is considered here as the baseline. By assigning an eccentricity to the circular isogrid cylinder, an elliptical isogrid cylinder of the same circumference, and therefore the same weight, results, but the axial buckling capacity is considerably reduced relative to the circular case. This is due to the fact that for a noncircular cross section the circumferential location with the largest radius of curvature attains its axial buckling capacity at a load lower than any other circumferential location. To mitigate the reduction in axial buckling capacity, the lattice rib angle is varied with circumferential location so that each circumferential location attains its buckling capacity at the same level of compressive strain. The analysis developed to proscribe the rib angle variation with circumferential location is based on representing the lattice cylinders as equivalent orthotropic cylinders, with the homogenized orthotropic material properties depending upon rib angle, rib modulus, and rib cross-sectional dimensions. By combining the known variation of the radius of curvature with circumferential location around the elliptical cylinders with a one-dimensional equation for the buckling stress of an orthotropic circular cylinder, variable rib angle elliptical lattice cylinders are designed. Though the variable rib angle elliptical lattice cylinder does not fully recover the buckling capacity of the baseline isogrid circular cylinder, it does outperform the elliptical isogrid cylinder. Results from a finite element analysis compare well with the predictions of the developed analysis. Three levels of eccentricity and two overall cylinder sizes are considered to illustrate the generality of the findings. It is fully expected that the approach developed is applicable to other noncircular cross-sectional geometries.

Nomenclature

a = major radius of ellipse, m
a_c = circumferential rib spacing, m
a_h = helical rib spacing, m
b = minor radius of ellipse, m
c = circular
cr = critical
d_c = width of circumferential ribs, m
d_h = width of helical ribs, m
E = geometric mean isotropic Young's modulus, pa
E_1 = Young's modulus in x_1-direction, Pa
E_2 = Young's modulus in x_2-direction, Pa
E_r = Young's modulus of rib, pa
e = eccentricity
e_{12} = E_1/E_2
G = geometric mean isotropic shear modulus, pa
G_{12} = shear modulus in x_1-x_2 plane, pa
g_{12} = G_{12}/G
h = thickness of cylinder wall lattice, m
h = thickness of cylinder wall lattice, m
K = correction factor for rib density
L = length of cylinder, m
l_h = length of helical ribs, m
N = axial stress resultant, N/m
n_c = number of circumferential ribs
n_h = number of helical ribs
P = axial load, n
Q_{ij} = reduced stiffness, N/m
R = radius of curvature, m
s = arc length, m
t = elliptical parameter, Eq. (18)
V = volume, m^3
X = x evaluated for $s = 2\pi R_c$, m, Eq. (51)
x = axial position along a helical rib, m
α_φ = ϵ_0/η_c
δ = rib density, d_c/a_c
$\mathcal{E}$ = normalized complete elliptical integral of second kind
ϵ_0 = axial strain
η = h/R
ν = geometric mean isotropic Poisson's ratio
ν_{12} = major Poisson's ratio
ρ = R/R_c
σ = axial stress, pa
φ = function of material properties, Eq. (28)
ϕ = helical rib angle, rad

Presented as Paper 2010-2703 at the 51st AIAA/ASME/ASCE/AHS/ASC Structures, Structural Dynamics, and Materials Conference, Orlando, FL, 12–15 April 2010; received 17 June 2010; revision received 16 September 2010; accepted for publication 20 September 2010.

*Post-Ph.D., INFOCOM Department, Polo per la Mobilità Sostenibile (POMOS) Laboratories; maurizio.paschero@pomos.it.

†N. Waldo Harrison Professor, Department of Engineering Science and Mechanics; hyerm@vt.edu. Fellow AIAA.

I. Introduction

LATTICE construction often used in aerospace structures consists of a network of relatively small beamlike elements joined at their ends to form a repeating pattern of triangles that, in turn, form a plate, cylinder, or other structural component. The classic isogrid lattice concept is based on each triangle being equilateral and therefore with an included angle between the beams, or ribs, of 60 deg. With this rib angle the homogenized in-plane

elastic properties of a lattice plate, for example, are the same in all directions, hence the prefix "iso." The cross-sectional dimensions and the axial modulus of the ribs, as well as the overall dimensions of the basic triangle, control the homogenized elastic properties of the lattice. An isogrid lattice can be sandwiched between two thin layers of material to form a sandwich structure with the lattice as a stiffening core. If the sandwiching layers are isotropic, then the homogenized elastic properties of the sandwich are isotropic. The structural efficiency and potential of the isogrid lattice concept motivated the development of design guide a number of years ago [1]. Since then, interest has continued and more generalized grids and lattices have been investigated, particularly analysis methodologies, but also manufacturing approaches. Various methods of representing the latticelike and repetitive nature of the large orbiting space structures being considered at that time were summarized in 1988 by Noor [2]. In 1996 Chen and Tsai [3] summarized methods for computing the response of planar grid structures and presented an equivalent stiffness model for representing so-called orthogrids and angle-grids that included a more refined representation of the response of the individual ribs. Hohe and Becker [4] and Hohe et al. [5] used energy methods to develop effective elastic properties of triangular, hexagonal, and quadrilateral grids, while Kim [6] considered isogrid cylinders.

When the rib angle of a planar triangular grid assumes values different than 60 deg, the structure does not exhibit isotropic elastic behavior. For this reason these structures are usually referred to as anisogrid lattice structures. Vasiliev et al. [7] outlined the basic design concepts and industrial fabrication methods for anisogrid lattice structures, together with a description of experimental testing and the serial development methodologies in Russia. Analogous progress in the fabrication, analysis, and design methods of anisogrid stiffened structures achieved mostly in the United States is reported by Huybrechts et al. [8]. More recently Hualin and Wei [9] studied lattice structures wherein the yield stress of the grid material was used to construct yield surfaces of the lattice when subjected to various loadings, with consideration given to rib buckling when compression was an issue. Li and Chen [10] studied planar grid structures by using classical plate theory and assuming the plate had discontinuous material properties represented by Heaviside step functions. Fan et al. [11] conducted an experimental investigation of sandwich panels with so-called Kagome-grid cores. Kagome grids refers to grids designed so no more than two ribs cross at a point, even though there are more than two rib angles. Considering again rib failure by yielding or buckling, Fan et al. [12,13] developed failure surfaces of isogrid, Kagome-grid, and diamond-grid structures subjected to uniaxial, shear, and hydrostatic loadings. Post-yield behavior was modeled by using Ramberg–Osgood relations to represent rib stress-strain response. It was shown that although the in-plane elastic behavior of isogrid structures is isotropic, the failure behavior is anisotropic. To that end, Fan and Fang [14] studied lattice symmetries and their effect on anisotropic properties. Parameters defined as the ratios of the maximum to minimum stiffness and strength, where the maximum and minimum values were identified with particular directions, were used to compare various grid designs. There are disadvantages to lattice structures that have slowed their development, not the least of which is the difficulty in fabricating such structures, particularly where the ribs join. Repair of a lattice structure is also an issue, though it could be argued that a lattice-stiffened structure is more damage tolerant than a conventionally stiffened structure.

Not directly related to lattice structures, there has recently been interest in tailoring the wall properties of thin-walled cylinders as a function of circumferential location to offset a geometric effect or to better react a particular applied load. Paschero and Hyer [15] improved the axial buckling capacity of an isotropic cylinder with an elliptical cross section by varying wall thickness with circumferential location. Considering the particulars in that study, the axial buckling load of an isotropic cylinder with an elliptical cross section, a uniform wall thickness, and an aspect ratio of 0.7, aspect ratio being defined as the ratio of the minor cross-sectional dimension to the major cross-sectional dimension, is approximately 40% less than that of a circular cylinder with the same circumference, same uniform wall thickness, same length, same material, and therefore, the same mass. The buckling capacity of the elliptical cylinder with a variable wall thickness was made to match that of a circular cylinder of the same circumference and weight. To improve the performance of a thin-walled fiber-reinforced composite circular cylinder in bending, Blom et al. [16] varied fiber orientation continuously with circumferential location to tailor the material properties as the stress state varied continuously from maximum tension to maximum compression around the circumference. Blom et al. [17] also varied with axial location the fiber orientation in a conical circular cylinder to compensate for the changing radius of curvature with axial location and maximize the fundamental frequency. Sun and Hyer [18] varied with circumferential location the fiber angle θ, measured relative to the axial direction, in the $[\pm\theta/0/90]_{2S}$ wall laminate of an elliptical fiber-reinforced cylinder in order to improve the axial buckling load relative to a quasi-isotropic wall elliptical cylinder, i.e., $\theta = 45$ deg, with no increase in weight.

Building on this past work and continuing to investigate the gains that can be achieved by material property tailoring concepts such as have been described, in the present work the rib angle of an elliptical cylinder constructed of a single layer of triangular lattice construction is varied with circumferential location in order to improve its axial buckling capacity. As with the preceding elliptical cylinder examples, an elliptical isogrid cylinder has less axial buckling capacity than a circular isogrid cylinder of the same thickness, circumference, and length. The key objective of the work is to determine how the rib angle should be varied with circumferential location around the ellipse. This is unlike the grid studies mentioned previously where grid geometry did not vary with position in the structure. As shown in Sec. III, as the included rib angle in this single layer elliptical cylinder studied here deviates from 60 deg, the homogenized material behaves as an orthotropic material. Consequently the terminology orthogrid construction is adapted, though this terminology is used by some to mean the ribs intersect at 90 deg. angles [3]. It should be noted that elliptical cross sections are of interest mainly because the geometry of an ellipse can be described conveniently, but the development presented is applicable to any noncircular cross section.

The paper continues in Sec. II with the introduction of the expressions for the axial buckling stress of a homogeneous circular orthotropic cylinder. These expressions form the basis for the analysis developed in this study for determining rib angle variation with circumferential location. The axial buckling stress is expressed in terms of the engineering properties of the geometric mean isotropic (GMI) material associated with the orthotropic material. In Sec. III the expressions for the equivalent homogenized orthotropic elastic properties of an orthogrid lattice structure are presented. A key variable in these expressions is, of course, the lattice rib angle. In Sec. IV the expressions for the homogenized elastic properties of the orthogrid lattice are then combined with the expressions for the axial buckling stress of a homogenous circular orthotropic cylinder to develop expressions for the axial buckling stress of a circular cylinder of orthogrid construction. In Sec. V the geometry of elliptical cross sections is introduced and in Sec. VI the reduced buckling capacity of elliptical cross section cylinders quantified. Then, the various assumptions, steps, and calculations required for the analysis to determine the rib angle variation with circumferential location around an elliptical lattice cylinder are discussed in Sec. VII. Predictions of improved axial buckling capacity of cylinder designs based on the developed analysis are presented. Details of the lattice designs are discussed in Sec. VIII. Finally, in Sec. IX the improved axial buckling performances of cylinders with three levels of eccentricity and two overall sizes as predicted by the developed analysis are compared with results based on finite element analyses.

II. Axial Buckling Capacity of a Circular Orthotropic Cylinder

Consider a geometrically perfect, homogeneous, thin-walled elastically orthotropic circular cylinder of radius R and wall

thickness h that is axially compressed on one end by either a stress or a displacement that is circumferentially uniform, the other end being held fixed. In either case the state of stress in the cylinder is primarily unidirectional in the axial direction and the axial buckling, or critical, stress can be estimated by [19]

$$\sigma_{\rm cr}(g_{12}) = \begin{cases} \frac{Eh\sqrt{g_{12}}}{R\sqrt{3(1-\nu^2)}} & \text{for } 0 < g_{12} < 1 \\ \frac{Eh}{R\sqrt{3(1-\nu^2)}} & \text{for } g_{12} \geq 1 \end{cases} \tag{1}$$

where the GMI properties associated with the given orthotropic material are defined as

$$E = \sqrt{E_1 E_2} \qquad \nu = \sqrt{\nu_{12}\nu_{21}}$$
$$G = \frac{E}{2(1+\nu)} = \frac{\sqrt{E_1 E_2}}{2(1+\sqrt{\nu_{12}\nu_{21}})} \tag{2}$$

with the constraints that

$$E > 0 \qquad \nu^2 - 1 < 0 \qquad G > 0 \tag{3}$$

Additionally, two nondimensional parameters are defined as

$$e_{12} = \frac{E_1}{E_2} \qquad g_{12} = \frac{G_{12}}{G} \tag{4}$$

As a result of these relations, the orthotropic elastic properties of the cylinder wall can be written as

$$E_1 = \sqrt{e_{12}}E \qquad E_2 = \frac{E}{\sqrt{e_{12}}} \qquad \nu_{12} = \sqrt{e_{12}}\nu \qquad \nu_{21} = \frac{\nu}{\sqrt{e_{12}}}$$
$$G_{12} = \frac{g_{12}E}{2(1+\nu)} \tag{5}$$

where E_1 is the modulus of the orthotropic material in the axial, or 1, direction, E_2 is the modulus in the circumferential, or 2, direction, ν_{12} is the major Poisson's ratio of the material, and G_{12} is its in-plane shear modulus. As seen, the right-hand side of (1) depends upon the value of g_{12}. When $0 < g_{12} < 1$ the wall material is softer in shear than the associated GMI material, so-called undershear GMI, and the cylinder buckles in a nonaxisymmetric deformation pattern. When $g_{12} > 1$ the wall material is stiffer in shear than the associated GMI material, so-called over-shear GMI, the cylinder buckles in an axisymmetric deformation pattern, and the buckling capacity does not depend upon shear modulus. For the case of $g_{12} \geq 1$ the expression for the axial buckling stress is identical to that for an isotropic circular cylinder [20,21], wherein the Young modulus and the Poisson ratio of the isotropic material replace those of the GMI material with orthotropic material properties. The axial strain at buckling can be easily computed using the axial modulus and (1). The simplicity of (1) is due to the fact that buckling of cylinders usually begins in the membrane region, so cylinder length and the specific boundary conditions are generally not important.

Equation (1) works well for the case of a noncircular cylinder if the maximum radius of curvature of the cross section $R_{\rm max}$ is substituted for the radius R [18,22]. And therein lies the Achilles heel of a noncircular cross section. That is, axial buckling is controlled by the radius of curvature of the flattest portion of the cross section, while the remainder of the material in the cross section is understressed, in the sense of buckling, and therefore underused. More will be said of this shortly.

III. Orthogrid Lattice Construction

The particular orthogrid lattice construction considered in the present work is shown schematically in Fig. 1. As applied to a cylinder, the orthogonal directions x_1 and x_2 illustrated are the axial and circumferential directions, respectively, of the cylinder. The lattice is of thickness h in the x_3 direction (not shown) and the x_1-x_2 cylindrical surface is located midthickness of the lattice. With the construction shown in Fig. 1 there are pairs of helical ribs oriented at

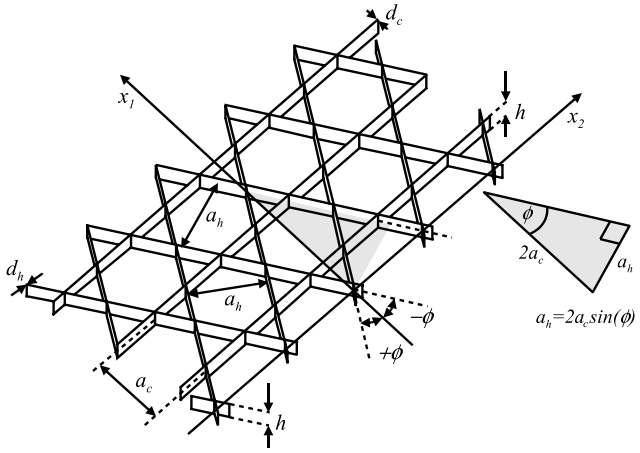

Fig. 1 Lattice construction considered here.

angles $\pm\phi$ relative to the axial direction. The spacings of the circumferential and helical ribs are, respectively, a_c and a_h and the rib widths are d_c and d_h. With the arrangement of Fig. 1 the elastic properties of the lattice can be represented as an equivalent homogenized orthotropic material with properties E_1, E_2, ν_{12}, and G_{12}. These equivalent orthotropic properties are functions of the rib axial modulus, rib spacing, rib cross-sectional area, and importantly, rib angle. According to [23] a lattice layer of specular helical ribs with axial modulus E_r, cross-sectional area $h \times d_h$, forming angles ϕ with the coordinate line x_1 (see Fig. 1) can be considered as a continuum layer having equivalent reduced stiffnesses given by

$$Q_{11} = 2\frac{E_r d_h}{a_h}\cos^4(\phi) \tag{6a}$$

$$Q_{22} = 2\frac{E_r d_h}{a_h}\sin^4(\phi) \tag{6b}$$

$$Q_{12} = Q_{21} = 2\frac{E_r d_h}{a_h}\cos^2(\phi)\sin^2(\phi) \tag{6c}$$

$$Q_{33} = 2\frac{E_r d_h}{a_h}\cos^2(\phi)\sin^2(\phi) \tag{6d}$$

Considering the circumferential ribs and superposing effects, the equivalent reduced stiffnesses of the lattice in Fig. 1 are given by

$$Q_{11} = 2\frac{E_r d_h}{a_h}\cos^4(\phi) \tag{7a}$$

$$Q_{22} = 2\frac{E_r d_h}{a_h}\sin^4(\phi) + \frac{E_r d_c}{a_c} \tag{7b}$$

$$Q_{12} = Q_{21} = 2\frac{E_r d_h}{a_h}\cos^2(\phi)\sin^2(\phi) \tag{7c}$$

$$Q_{33} = 2\frac{E_r d_h}{a_h}\cos^2(\phi)\sin^2(\phi) \tag{7d}$$

This homogenization scheme is known to work well for buckling problems.[‡]

To improve the local buckling capabilities, the length of each unsupported segment of a rib in the grid must be made as short as possible. One approach to achieve this condition is obtained by attaching the circumferential ribs at the middle point between two adjacent joints of helical ribs, as shown in Fig. 1, resulting in a Kagome-type grid [11]. It should be noted that this special geometry

[‡]Vasiliev, V. V., private communication.

of the grid produces the following constraint equation between the spacing dimensions a_h and a_c:

$$a_h = 2a_c \sin(\phi) \tag{8}$$

Assuming all the ribs to have the same width (i.e., $d_h = d_c$), a dimensionless parameter representing rib density can be defined as follows:

$$\delta = d_c/a_c \tag{9}$$

Substituting (8) and (9) in (7) results in equivalent reduced stiffness which can be written as

$$Q_{11} = E_r\delta\frac{\cos^4(\phi)}{\sin(\phi)} \tag{10a}$$

$$Q_{22} = E_r\delta(\sin^3(\phi) + 1) \tag{10b}$$

$$Q_{12} = Q_{21} = E_r\delta\cos^2(\phi)\sin(\phi) \tag{10c}$$

$$Q_{33} = E_r\delta\cos^2(\phi)\sin(\phi) \tag{10d}$$

Using (10), the equivalent engineering properties of the homogenized orthogrid can be obtained as

$$E_1 = Q_{11} - \frac{Q_{12}^2}{Q_{22}} = E_r\delta\left(\frac{\cos^3(\phi)\cot(\phi)}{1+\sin^3(\phi)}\right) \tag{11a}$$

$$E_2 = Q_{22} - \frac{Q_{12}^2}{Q_{11}} = E_r\delta \tag{11b}$$

$$\nu_{12} = \frac{Q_{12}}{Q_{22}} = \frac{\cos^2(\phi)\sin(\phi)}{1+\sin^3(\phi)} \tag{11c}$$

$$\nu_{21} = \frac{Q_{12}}{Q_{22}} = \tan^2(\phi) \tag{11d}$$

$$G_{12} = Q_{33} = E_r\delta\cos^2(\phi)\sin(\phi) \tag{11e}$$

Note that the isogrid case (i.e., $\phi = \pi/6$) results in

$$E_1 = E_2 = E_r\delta \qquad \nu_{12} = \nu_{21} = \frac{1}{3} \qquad G_{12} = \frac{3}{8}E_r\delta \tag{12}$$

where it is observed that the important parameters are rib axial modulus E_r and rib density δ.

IV. Axial Buckling Capacity of an Orthogrid Circular Cylinder

Substituting the equivalent orthotropic engineering properties of an homogenized orthogrid layer, (11), into the definitions of the GMI material, (2), results in

$$E = \sqrt{E_1E_2} = E_r\delta\sqrt{\frac{\cos^3(\phi)\cot(\phi)}{1+\sin^3(\phi)}} \tag{13a}$$

$$\nu = \sqrt{\nu_{12}\nu_{21}} = \sqrt{\frac{\sin^3(\phi)}{1+\sin^3(\phi)}} \tag{13b}$$

$$G = \frac{E}{2(1+\nu)} = E_r\delta\frac{\cos^2(\phi)}{2(\sin^2(\phi)+\sqrt{1+\sin^4(\phi)})} \tag{13c}$$

Similarly, the dimensionless parameters e_{12} and g_{12}, defined in (4), can be specialized for an orthogrid as

$$e_{12} = \frac{E_1}{E_2} = \frac{\cos^3(\phi)\cot(\phi)}{1+\sin^3(\phi)} \tag{14a}$$

$$g_{12} = \frac{G_{12}}{G} = 2\sin(\phi)(\sin^2(\phi) + \sqrt{\sin(\phi)+\sin^4(\phi)}) \tag{14b}$$

These expressions can substituted into (1) to compute the axial buckling stress of a circular orthogrid cylinder. However, the right-hand side of (1) depends upon the value of g_{12}, so the range of validity of each portion of the right-hand side of (1) can be expressed in terms of the rib angle ϕ as

$$0 \le g_{12} < 1 \Rightarrow 0 \le \phi < \pi/6 \qquad g_{12} > 1 \Rightarrow \pi/6 < \phi < \pi/2 \tag{15}$$

Consequently, the axial buckling stress of a circular orthogrid cylinder can be expressed as a function of rib angle as follows:

$$\sigma_{\rm cr}(\phi) = \begin{cases} E_r\delta\frac{h}{R}\cos^2(\phi)\sqrt{\frac{2}{3}(\sin^2(\phi)+\sqrt{\sin(\phi)+\sin^4(\phi)})} & \text{for } 0<\phi<\frac{\pi}{6} \\ E_r\delta\frac{h}{R}\frac{\cos^2(\phi)}{\sqrt{3\sin(\phi)}} & \text{for } \frac{\pi}{6}<\phi<\frac{\pi}{2} \end{cases} \tag{16}$$

When $\phi = \pi/6$ the orthogrid becomes an isogrid with Young's modulus $E_r\delta$ and Poisson's ratio $1/3$ [see (12) and (16)] assumes the following form:

$$\sigma_{\rm cr}(\pi/6) = \frac{1}{2}\sqrt{\frac{3}{2}}E_r\delta\frac{h}{R} = \frac{h(E_r\delta)}{R\sqrt{3(1-(1/3)^2)}} \tag{17}$$

Note the similarity of the right-hand side of (17) to the form of (1).

V. Cross-Sectional Geometry of an Ellipse

Consider a circular cylindrical shell with radius R_c, constant thickness h_c, and length L_c, the subscript c denoting circular. Suppose the given circular cross section is made elliptical by assigning to it an eccentricity e_0, but the circumference is kept the same as the original circular cylinder, namely $2\pi R_c$. An elliptical cross section can be described parametrically using the parameter t by the radius vector $\mathbf{v}(t)$ defined by

$$\mathbf{v}(t) = (a\cos(t), b\sin(t)) \qquad t \in [0, 2\pi) \tag{18}$$

where, as illustrated in Fig. 2, a and b are the semimajor and semiminor axes of the cross section of the midsurface and, as shown, $R(t)$, and h are the radius of curvature and the wall thickness. Also shown in Fig. 2 are circumferential locations corresponding to various values of t and the arc length coordinate s. The eccentricity of an ellipse e is defined as

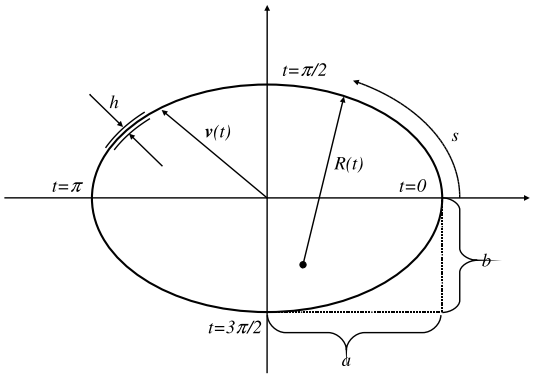

Fig. 2 Cross section of midsurface of elliptical cylinder.

$$e = \sqrt{1 - \frac{b^2}{a^2}} \tag{19}$$

It should be noted that $e = 0$ when $b = a$, the ellipse degenerating to a circle. Similarly, $e = 1$ when $b = 0$, the ellipse degenerating to a flat panel. Based on these arguments, it should be clear that in order to have an ellipse the following relation must be fulfilled: $0 \leq e < 1$. All the expressions involving the eccentricity derived in the following are meaningful only for this range of values.

The radius of curvature of the elliptical cross section can be expressed as a function of the parameter t as

$$R(t) = \frac{(b^2\cos^2(t) + a^2\sin^2(t))^{\frac{3}{2}}}{ab} \qquad t \in [0, 2\pi) \tag{20}$$

The semimajor radius a and the semiminor radius b of an ellipse having an assigned eccentricity e_0 and the same circumference as the original circular cylinder are given by

$$a = \frac{R_c}{\mathcal{E}(e_0^2)} \qquad b = \frac{R_c}{\mathcal{E}(e_0^2)}\sqrt{1 - e_0^2} \tag{21}$$

where $\mathcal{E}(.)$ is the normalized complete elliptical function of second kind defined by

$$\mathcal{E}(k) = \frac{2}{\pi}\int_0^{\frac{\pi}{2}} \sqrt{1 - k\sin^2(\theta)}\, \mathrm{d}\theta \tag{22}$$

It should be noted that when the assigned eccentricity $e_0 = 0$ (i.e., the circular case), (21) gives correctly $a = R_c$ and $b = R_c$, while when $e_0 = 1$ (i.e., the flat plate case), (21) gives correctly $a = \pi R_c/2$ and $b = 0$.

The radius of curvature $R(t)$ of an ellipse having the same circumference as the original circle and an assigned eccentricity e_0 can be obtained by substituting (21) in (20), that is,

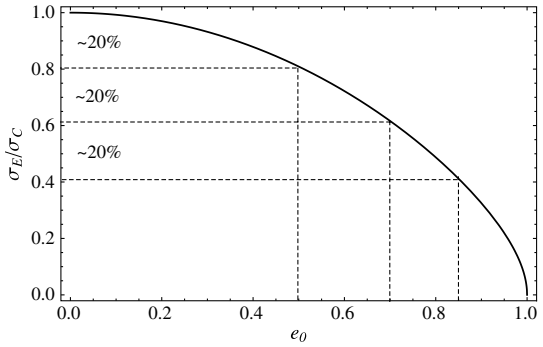

Fig. 3 Comparison between the buckling stress of elliptical and original circular cylinders.

$$R(t, e_0) = \frac{R_c}{\mathcal{E}(e_0^2)}\sqrt{\frac{(1 - e_0^2\cos^2(t))^3}{1 - e_0^2}} \qquad t \in [0, 2\pi) \tag{23}$$

The minimum and the maximum radii of curvature are given by the following relations:

$$\begin{aligned} R_{\min} &= R(0) = R(\pi) = \frac{R_c}{\mathcal{E}(e_0^2)}(1 - e_0^2) \\ R_{\max} &= R\left(\frac{\pi}{2}\right) = R\left(\frac{3\pi}{2}\right) = \frac{R_c}{\mathcal{E}(e_0^2)}\frac{1}{\sqrt{1 - e_0^2}} \end{aligned} \tag{24}$$

VI. Reduction of Capacity of Elliptical Cross Section

Based on the arguments stated at the end of Sec. II regarding using $R_{\max}$ of a noncircular cylinder in (1) and (24) can be used to compute the reduction in axial buckling capacity of an elliptical orthotropic or isotropic cylinder as compared with a circular cylinder of the same uniform wall thickness and circumference. Using (1) and (24), the ratio of the axial buckling stress of the elliptical cylinder, σ_E, to the axial buckling stress of the circular cylinder, σ_C, can be written as

$$\frac{\sigma_E}{\sigma_C} = \frac{R_c}{R_{\max}} = \mathcal{E}(e_0^2)\sqrt{1 - e_0^2} \tag{25}$$

This ratio is plotted in Fig. 3 to illustrate the reduction in axial buckling stress as a function of eccentricity of the elliptical cross section. As seen, the buckling stress of a elliptical cylinder decreases considerably with increasing eccentricity. For example, about 20% of the stress level is lost when an eccentricity of 0.50 is assigned to the original circular cylinder. Similarly about 40% of the stress level is lost for $e_0 = 0.70$ and about 60% for $e_0 = 0.85$.

For completeness, the deformed shapes of circular and elliptical thin-walled simply supported cylinders with the same circumferences, wall thicknesses, and lengths compressed by circumferentially uniform axial displacements to levels just slightly less than their respective buckling levels are shown in Fig. 4. The eccentricity of the elliptical cylinder is 0.70 and S1 simple support boundary conditions [21] are enforced. These deformed shapes are representative of both isotropic and orthotropic materials, as long as the wall stiffness properties are independent of circumferential and axial location. As seen in Fig. 4, the deformations are confined primarily to the boundary layers at the ends of the cylinders, but the deformations of the elliptical cylinder are further confined to the flatter portions of the cylinder cross section. In fact, the more curved portions of the elliptical cross section are hardly deformed. This implies that the material in the more highly curved portions is not being used to its fullest extent, at least in the context of axial buckling. To increase the axial buckling stress relative to the decreases illustrated in Fig. 3, the variable thickness design elliptical cylinders of Paschero and Hyer [15] featured a continuous change of wall thickness with circumferential location that resulted in a thinning of

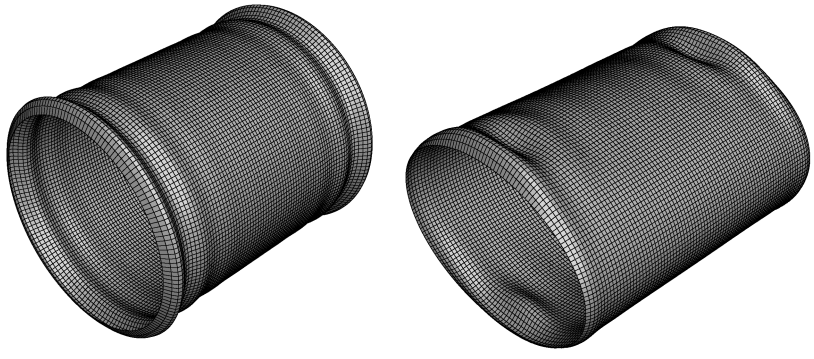

a) b)

Fig. 4 Prebuckling deformed shape of axially loaded simply supported cylindrical shells: a) circular cross section and b) elliptical cross section $e_0 = 0.70$.

the wall in the more highly curved portions of the cross section and a thickening in the flatter regions. The total amount of material in the resulting variable thickness design was equal that of the circular case.

VII. Improving the Axial Buckling Capacity of an Orthogrid Elliptical Cylinder

Rather than vary wall thickness, or in the situation here, rib thickness, to tailor stiffness properties with circumferential location to improve the axial buckling capacity of an elliptical cylinder, as was done in Paschero and Hyer [15], in the present paper the material properties are to be tailored by varying the rib angle of the orthogrid cylinder with circumferential location. A scheme is needed to proscribe the rib angle variation. To that end, it is assumed that for the case of a noncircular cylinder (1) is valid locally. That is, the critical axial stress at each circumferential location is controlled by the material properties, radius of curvature, and wall thickness at that circumferential location. Moreover, there is a circumferential location where the local values of the material properties, radius of curvature, and wall thickness in (1) result in the lowest critical axial stress value and thereby control buckling. To build upon this assumption, consider an isogrid lattice circular cylinder of radius R_c and wall thickness h_c, herein considered the baseline and denoted as an isogrid circular (IGC) cylinder. Consider also an elliptical orthogrid cylinder of the same thickness with eccentricity e_o, the same circumference as the IGC cylinder ($2\pi R_c$), and for which the rib angle, and thus the material properties, in (1) vary with the elliptical parameter t of Fig. 2. This cylinder will be referred to as the variable grid elliptical (VGE) cylinder. For the VGE cylinder (1) can thus be written

$$\sigma_{\mathrm{cr}}(t,e_0)=\begin{cases}\frac{E(t,e_0)h_c\sqrt{g_{12}(t,e_0)}}{R(t,e_0)\sqrt{3(1-\nu^2(t,e_0))}} & \text{for } 0<g_{12}(t,e_0)<1\\ \frac{E(t,e_0)h_c}{R(t,e_0)\sqrt{3(1-\nu^2(t,e_0))}} & \text{for } g_{12}(t,e_0)\geq 1\end{cases} \tag{26}$$

For convenience of notation Eq. (26) can be rearranged as

$$\sigma_{\mathrm{cr}}(t,e_0)=\eta_c\left(\frac{\varphi(t,e_0)}{\rho(t,e_0)}\right)E_1(t,e_0) \tag{27}$$

where the function $\varphi(t,e_o)$ depends only on material parameters and is given by

$$\varphi(t,e_0)=\begin{cases}\sqrt{\frac{g_{12}(t,e_0)}{3e_{12}(t,e_0)(1-\nu^2(t,e_0))}} & \forall\ t\in[0,2\pi)\text{: } 0<g_{12}(t,e_0)<1\\ \frac{1}{\sqrt{3e_{12}(t,e_0)(1-\nu^2(t,e_0))}} & \forall\ t\in[0,2\pi)\text{: } g_{12}(t,e_0)\geq 1\end{cases} \tag{28}$$

The dimensionless function $\rho(t,e_0)$ depends only on the radius of curvature of ellipse and using (23) is defined by

$$\rho(t,e_0)=\frac{R(t,e_0)}{R_c}=\frac{1}{\mathcal{E}(e_0^2)}\sqrt{\frac{(1-e_0^2\cos^2(t))^3}{1-e_0^2}}\qquad t\in[0,2\pi) \tag{29}$$

The scalar variable η_c is a dimensionless parameter defined by

$$\eta_c=\frac{h_c}{R_c} \tag{30}$$

Assuming that the elliptical cylinder is compressed on one end by an axial displacement that is uniform around the circumference, the state of stress in the cylinder is very much uniaxial and is given by

$$\sigma(t,e_0)=E_1(t,e_0)\epsilon_0\quad\forall\ t\in[0,2\pi) \tag{31}$$

where ϵ_0 is the uniform strain state in the elliptical cylinder produced by the circumferentially uniform axial displacement. By requiring that every circumferential location in the elliptical cylinder be stressed to its critical level, not just the flatter region of the cross section (see Fig. 4), the actual state of stress in the cylinder, (31), is equated to the critical stress at that location, (27). This requirement can be written as

$$\sigma(t,e_0)=\sigma_{\mathrm{cr}}(t,e_0)\quad\forall\ t\in[0,2\pi) \tag{32}$$

Substituting (27) and (31) into (32), rearranging, and eliminating $E_1(t,e_o)$ from both sides, the design condition can be written as

$$\eta_c\frac{\varphi(t,e_0)}{\rho(t,e_o)}=\epsilon_0\Rightarrow\varphi(t,e_0)=\alpha_\varphi\rho(t,e_o)\quad\forall\ t\in[0,2\pi) \tag{33}$$

where α_φ is a positive scalar quantity defined as

$$\alpha_\varphi=\frac{\epsilon_0}{\eta_c} \tag{34}$$

The design of the variable material property elliptical cylinder is complete once the value of the constant α_φ in (33) is specified.

All the arguments developed in this section until this point are valid for a noncircular cylinder made of an orthotropic material. In the rest of this section all the expressions derived will be specialized considering that the cylinder is made of an orthogrid material and that material property tailoring will result by varying the rib angle with circumferential location. Other approaches to tailoring material properties could be considered, for example using the concept of a functionally graded material [24].

To continue with the VGE cylinder design, the constant α_φ will be selected so the value of axial strain that produces buckling in the VGE cylinder is the same value that produces buckling in the IGC cylinder. Only that choice of α_φ will be considered here, though other choices could be considered. Using (12), (17), and (34) results in

$$\epsilon_0=\frac{\sigma_{\mathrm{cr}}(\pi/6)}{E_1(\pi/6)}=\eta_c\frac{1}{2}\sqrt{\frac{3}{2}}\Rightarrow\alpha_\varphi=\frac{\epsilon_0}{\eta_c}=\frac{1}{2}\sqrt{\frac{3}{2}} \tag{35}$$

Specializing (28) for the case of an orthogrid lattice, using (13) and (14), leads to

$$\varphi(\phi(t,e_0))=\begin{cases}\frac{1+\sin^3(\phi)}{\cos^2(\phi)}\sqrt{\frac{2}{3}(\sin^4(\phi)+\sqrt{\sin^5(\phi)+\sin^8(\phi)})} & 0<\phi<\frac{\pi}{6}\\ \frac{1+\sin^3(\phi)}{\cos^2(\phi)}\sqrt{\frac{1}{3}\sin(\phi)} & \frac{\pi}{6}\leq\phi<\frac{\pi}{2}\end{cases} \tag{36}$$

where, for brevity of notation, the dependence of the function on the circumferential location and the assigned eccentricity through the rib angle [i.e., $\phi(t,e_0)$] is highlighted on the left side of the equation only. The function in (36) is plotted in Fig. 5. Based on Fig. 5, a few comments can be made regarding (36). First, as expected, the function exhibits an inflection point at $\phi=\pi/6$ due to the junction of the two parts of the equation at this value of ϕ (see Fig. 5b). Second, the function monotonically increases from zero to infinity (see Fig. 5a) when the rib angle ϕ is varied between zero, i.e., axial ribs, and $\pi/2$, i.e., circumferential ribs. Based on this argument, keeping in mind that when the assigned eccentricity is varied within its admissible range (i.e., $0\leq e_0<1$), the function $\rho(t,e_0)$ assumes only positive values and it is realized that (33) is solvable. Substituting (29) and (35) in (33) and evaluating the inverse function, the rib angle as a function of the circumferential location for each assigned eccentricity can be found. That function is given by

$$\phi(t,e_0)=\varphi^{-1}\left[\frac{1}{2\mathcal{E}(e_0^2)}\sqrt{\frac{3(1-e_0^2\cos^2(t))^3}{2(1-e_0^2)}}\right]\quad\forall\ t\in[0,2\pi) \tag{37}$$

Unfortunately, due to the transcendental nature of (36) the inverse function $\varphi^{-1}[.]$ cannot be analytically evaluated, except for the two limiting cases, $e_0=0$ and $e_0=1$. More precisely, setting $e_0=0$ in (37) the following relation is obtained

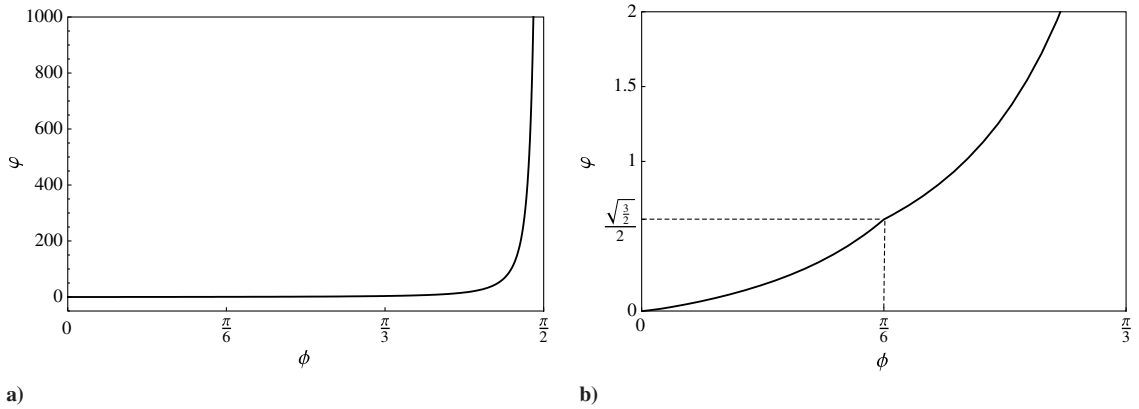

Fig. 5 φ vs ϕ: a) $0 \le \phi < \pi/2$ and b) $0 \le \phi \le \pi/3$.

$$\phi(t,0) = \varphi^{-1}\left[\frac{1}{2}\sqrt{\frac{3}{2}}\right] = \frac{\pi}{6} \qquad t \in [0, 2\pi) \tag{38}$$

Looking at Fig. 5b and keeping in mind that for $\rho(t,0) \equiv 1$ it is immediately seen that the solution of (38) is $\phi = \pi/6$. Equation (38) simply means that (33) correctly predicts that if no eccentricity is assigned to the IGC cylinder, then no adjustment to the rib angle is necessary. The second analytically solvable case can be studied taking the limit of (37) for e_0 approaching unity. The result is

$$\phi(t,1) = \lim_{e_0 \to 1} \phi(t, e_0) = \lim_{e_0 \to 1} \varphi^{-1}\left[\frac{1}{2\mathcal{E}(e_0^2)}\sqrt{\frac{3(1-e_0^2\cos^2(t))^3}{2(1-e_0^2)}}\right] = \begin{cases} 0 & t = 0, \pi \\ \frac{\pi}{2} & \text{otherwise} \end{cases} \tag{39}$$

Equation (39) means that when the IGC cylinder is squeezed into a flat panel, the ribs should be made circumferential at each point except the two edges, where the ribs should be axial. Of course these limiting cases have only a purely theoretical interest and should not be taken into consideration for practical implementation. Other than these two limiting cases, a numerical solution must be employed. Accordingly, (37) will be solved at 168 points corresponding to equispaced locations around the cylinder circumference. The 168 points correspond to the circumferential mesh density in the finite element model to be discussed in a subsequent section. The numerical solution of (37) is shown in Fig. 6, as a function of normalized circumferential arc length, for different values of assigned eccentricity.

A few comments can be made regarding Fig. 6. First, it can be noted that, as expected, the function $\phi(t, e_0)$ gradually varies between the two limiting functions $\phi(t,0)$ [see (38)] and $\phi(t,1)$ [see (39)]. More precisely, the variation is quite smooth when the assigned eccentricity is lower than about $e_0 = 0.9$ and changes very fast when $0.9 < e_0 < 1$. Second, the flatter regions of the ellipse, i.e., the regions around $s/2\pi R_c = 0.25$ and $s/2\pi R_c = 0.75$, are associated with rib angle values greater than $\phi = \pi/6$, which results in a softer axial modulus than in the IGC cylinder. Moreover, as discussed earlier, rib angles greater than $\phi = \pi/6$ correspond to a over-shear GMI material and an axisymmetric buckled shape. Conversely, the more curved regions of the ellipse, i.e., the regions around $s/2\pi R_c = 0$ and $s/2\pi R_c = 0.5$, are associated with rib angles lower than $\phi = \pi/6$. This results in a stiffer axial modulus than in the IGC cylinder, an undershear GMI material, and a nonaxisymmetric buckled shape. Finally, it is seen from the Fig. 6 that the more the assigned eccentricity increases, the more the axially soft regions in the flatter locations of the cross section enlarge, bordering the axially stiff regions at the more curved locations. Alternatively, the more the assigned eccentricity increases, the more the over-shear GMI regions enlarge, bordering the undershear GMI regions at the more curved locations. According with the previous arguments, the developed analysis predicts the VGE cylinder will buckle with one pattern in the flatter regions, which tend to enlarge as eccentricity approaches unity, and with another pattern in the more curved regions, which tend to shrink the more the eccentricity approaches unity. More precisely, the boundary between the axially soft, over-shear GMI flatter regions and the axially stiff, undershear GMI more curved regions is located where the radius of curvature of the VGE cylinder is equal to the radius of the IGC cylinder, R_c. For this location the material has the axial modulus and shear stiffness of the GMI material, in this case the isogrid lattice. The value t_{IGC} of the parameter t dividing the two different regions can be estimated by requiring $\rho(t, e_0) = 1$. The following result is obtained

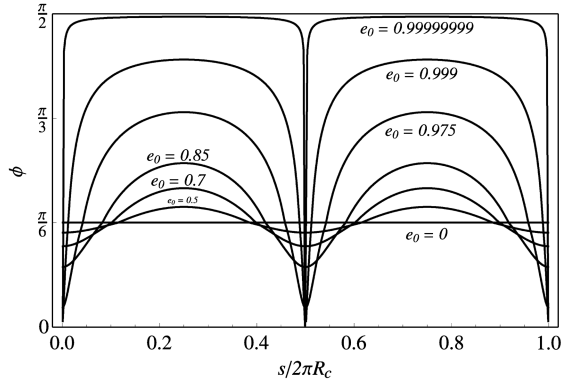

Fig. 6 Rib angle vs normalized circumferential location for different eccentricities.

$$t_{\text{IGC}}(e_0) = \arccos\left(\sqrt{\frac{1-((1-e_0^2)\mathcal{E}(e_0^2)^2)^{\frac{1}{3}}}{e_0^2}}\right) \tag{40}$$

Once the function $\phi(t, e_0)$ is known, the axial stress as a function of the circumferential location can be easily determined. In fact, it can be noted that when the rib angle is tailored using $\phi(t, e_0)$, by definition the strain level at the buckling condition is constant all around the cylinder circumference and consequently the following expression can be written for the axial stress around the circumference of the VGE cylinder at buckling:

$$\sigma_{\text{VGE}} = E_1(\phi(t, e_0))\epsilon_0 \qquad t \in [0, 2\pi) \tag{41}$$

Similarly, using (11) and (38) the axial buckling stress of the IGC cylinder can be determined to be

$$\sigma_{\text{IGC}} = E_1(\phi(t,0))\epsilon_0 = E_1(\pi/6)\epsilon_0 = E_r\delta\epsilon_0 \qquad t \in [0, 2\pi) \tag{42}$$

Dividing (41) by (42), the following expression is obtained:

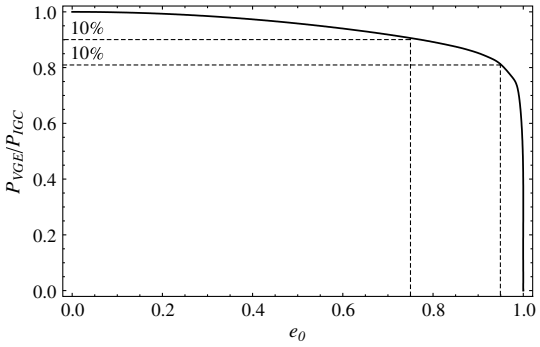

Fig. 7 Ratio $P_{\mathrm{VGE}}/P_{\mathrm{IGC}}$ vs assigned eccentricity.

$$\frac{\sigma_{\mathrm{VGE}}}{\sigma_{\mathrm{IGC}}} = \frac{E_1(\phi(t,e_0))\epsilon_0}{E_r\delta\epsilon_0} = \frac{\cos^3(\phi(t,e_0))\cot(\phi(t,e_0))}{1+\sin^3(\phi(t,e_0))} = e_{12}(\phi(t,e_0) \qquad t\in[0,2\pi) \tag{43}$$

Equation (43) states that the ratio $\sigma_{\mathrm{VGE}}/\sigma_{\mathrm{IGC}}$ can be estimated by means of the ratio between the axial Young's modulus of the VGE cylinder and the axial Young's modulus of the IGC cylinder. This ratio is independent of the constitutive and geometric properties of the cylinder other than the rib angle as a function of the circumferential location [i.e., $\phi(t,e_0)$]. Moreover, the ratio is coincident with the function $e_{12}(\phi)$ defined in (14). Since the rib material is homogeneous through the thickness, which is constant around circumference, (43) can be also used to predict the ratio between the axial stress resultants of the VGE and IGC cylinders. Symbolically, that ratio is

$$\frac{N_{\mathrm{VGE}}}{N_{\mathrm{IGC}}} = \frac{\sigma_{\mathrm{VGE}}}{\sigma_{\mathrm{IGC}}} = e_{12}(\phi(t,e_0)) \qquad t\in[0,2\pi) \tag{44}$$

The ratio between the load capacity of the VGE cylinder and the load capacity of the IGC cylinder can be estimated by integrating (44) around the cylinder circumference to give

$$\frac{P_{\mathrm{VGE}}}{P_{\mathrm{IGC}}} = \int_0^{2\pi}\frac{N_{\mathrm{VGE}}}{N_{\mathrm{IGC}}}\,\mathrm{d}t = \int_0^{2\pi} e_{12}(\phi(t,e_0))\,\mathrm{d}t \qquad t\in[0,2\pi) \tag{45}$$

It should be noted that (45) depends only on the assigned eccentricity e_0. Equation (45) is plotted in Fig. 7. Looking at Fig. 7 it is seen that the VGE cylinder is not able to completely recover the axial buckling load of the IGC cylinder. Despite that, it can be seen that the VGE cylinder is able to recover more than 90% of the axial buckling load of the IGC cylinder when the assigned eccentricity is less that about 0.75, and more than 80% when the assigned eccentricity is less that about 0.95. When the assigned eccentricity is more than 0.95, the axial buckling load performance of the VGE cylinder decays quickly and reaches zero for $e_0 = 1$. As seen in Fig. 3, for a IGE cylinder about 20% of the axial buckling load of the IGC cylinder is lost when an eccentricity of approximately 0.5 is assigned to the circular cross section. With the VGE design the loss is only about 5%. For higher levels of eccentricity the advantages of using a variable rib angle design are even greater.

VIII. Details of Lattice Designs

All the theoretical results achieved in Section VII are based on the homogenized model of the lattice structure described in Section III. This model is used to estimate the function $\phi(t,e_0)$ which describes the variation of the helical rib angle as a function of circumferential position and assigned eccentricity. As is well known, homogenized models neglect considerations concerning the geometry of the actual structure and take into consideration only equivalent material properties. To not ignore this simplification, in the present section some problems related with the actual geometry of the discrete grid associated with a given $\phi(t,e_0)$ function will be taken into consideration. In particular, issues regarding cylinder length, the construction of the grid, and the volume of the VGE cylinder, and therefore the weight, as compared with that of the IGC cylinder, are discussed.

A. Cylinder Length

It is important to show how the actual grid geometry of the lattice structure can be obtained by the knowledge of the function $\phi(s,e_0)$. This operation is not obvious because it involves many geometric compatibility issues. To avoid unnecessary complications, the cylinder will be unrolled onto the plane $(x/2\pi R_c, s/2\pi R_c)$, as in Fig. 8, where, consistent with previous notation, $x/2\pi R_c$ represents the axial position of the generic point belonging to a helical rib measured from the lower end of the cylinder normalized by the cylinder circumference, while $s/2\pi R_c$ represents the circumferential position of the generic point belonging to a helical rib, measured as shown in Fig. 2, normalized by the circumference. For an assigned eccentricity the following relation involving circumferential arc length s can be written (see Fig. 2):

$$\frac{\partial x(s,e_0)}{\partial s} = \cot(\phi(s,e_0)) \tag{46}$$

The function $x(s,e_0)$ can be obtained by integrating (46) in s. Denoting by $X(e_0)$ for a given eccentricity e_0 the axial position of the point on a generic helical rib reached by moving along the rib while making one revolution around the circumference, i.e., $X(e_0)= x(2\pi R_c, e_0)$, the following relation can be written:

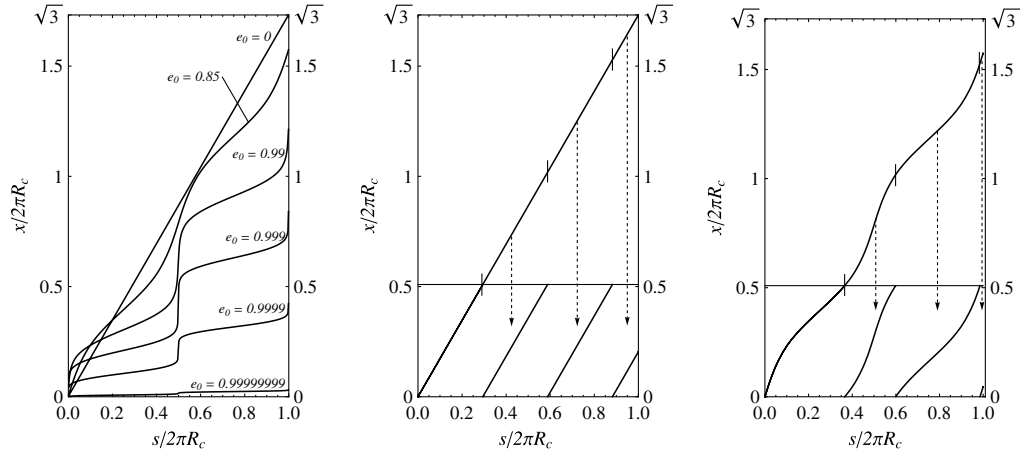

Fig. 8 Rib geometry: a) unrolled rib for different eccentricities, b) sectioned rib for $e_0 = 0$, and c) sectioned rib for $e_0 = 0.85$.

$$X(e_0) = \int_0^{2\pi R_c} \frac{\partial x(s, e_0)}{\partial s}\, \mathrm{d}s = \int_0^{2\pi R_c} \cot(\phi(s, e_0))\, \mathrm{d}s \qquad (47)$$

Stated differently, (47) is the furthest axial position from one end of the cylinder reached by moving along a generic helical rib while make one revolution around the circumference. In Fig. 8a are shown the helical ribs unrolled in the plane $(s/2\pi R_c, x/2\pi R_c)$ for different eccentricities. As seen from Fig. 8a the axial position furthest from one end of the cylinder, $X(e_0)/2\pi R_c$, has a maximum for $e_0 = 0$ equal to $\sqrt{3}$ and decreases the more the eccentricity increases until it becomes zero for $e_0 = 1$. The understanding of Fig. 8a illustrates that the length of the helical ribs varies from two times the circumferential length to one times the circumferential length as the assigned eccentricity e_0 varies from 0 to 1. The maximum axial position $X(e_0)$ for one revolution of the circumference is fixed once the function $\phi(s, e_0)$ has been determined. Unfortunately, $X(e_0)$ may not coincide with the required length of cylinder for a particular application, meaning that once the full length of helical rib has been rolled into a cylindrical shape, it reaches the axial position $X(e_0)$ that could likely be different than any specific required length of cylinder. Stated differently, when a helical rib is completely wrapped around the circumference, the cylinder must have a length $X(e_o)$. This inconvenience can, however, be easily resolved by realizing that the function $\phi(s, e_0)$ allocates a specific rib angle to each circumferential location, independently from the axial position of the ribs in the cylinder. This means that the helical ribs can be shifted axially without compromising the results obtained through the homogenized model of the lattice used to estimate the function $\phi(s, e_0)$. Based on these arguments, the helical ribs can be cut and shifted down axially each time a rib reaches the required length. This procedure is illustrated in Figs. 8b and 8c for $e_0 = 0$ and $e_0 = 0.85$, respectively. In the following this technique will be referred to as the "cut and shift" procedure. Unfortunately, this procedure is not enough to guarantee geometric compatibility within the lattice. In fact, assuming for convenience a mapping of the point $(s/2\pi R_c, x/2\pi R_c) = (0, 0)$ in Figs. 8b and 8c onto the point $(x_1, x_2) = (0, 0)$ in Fig. 1, in order to guarantee that each helical rib is continuous once the edge at $s/2\pi R_c = 0$ and the edge at $s/2\pi R_c = 1$ are joined together to form the cylindrical shape, it is a requirement that the maximum axial position of the last section of the rib which has its lower end at $s/2\pi R_c = 0$ in Figs. 8b and 8c must be equal to an integer multiple of the quantity $2a_c$ (where a_c, recall, is the spacing between two adjacent circumferential ribs). The previous requirement can be understood by looking at Fig. 1, where it is shown that in order to obtain the needed geometry, the intersections of the specular helical ribs must be spaced by a distance $2a_c$ along the x_1 direction (see hypotenuse of gray triangle). Moreover, looking at Fig. 1 it can be noted that the x_2 axis coincides with the points of intersection of the specular helical ribs, meaning that the described mapping results in the first set of intersection points lying on the lower end of the cylinder. It seems reasonable to design a structure with axial symmetry, so it is assumed that the last set of intersection points lies on the upper end of the cylinder. This prescription produces the requirement for the entire length of the cylinder to be a multiple of the quantity $2a_c$ and for the total number of circumferential ribs n_c to be an even number. The requirement to have helical rib intersection points that correspond to the upper and lower ends of the cylinder makes it generally impossible to construct a lattice cylinder of any particular required length. On the other hand, this prescription allows for the construction of the entire lattice cylinder by simply joining together $n_c/2$ (remember n_c is even) fundamental strips of axial dimension $2a_c$. The procedure to construct a fundamental strip and the entire lattice cylinder will be discussed in the following subsection.

To select the length L which is as close as possible to the desired cylinder length L_c and which is geometrically compatible, a few steps are needed. Once the number of circumferential ribs n_c to include in the structure is known, the ideal spacing $(a_c)_{\text{ideal}}$ among ribs can be estimated by

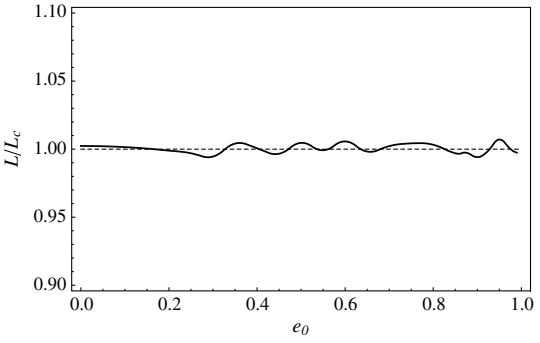

Fig. 9 Ratio L/L_c vs assigned eccentricity for $n_c = 30$.

$$(a_c)_{\text{ideal}} = \frac{L_c}{n_c} \qquad (48)$$

As stated previously, to obtain the needed geometry the entire axial length $X(e_0)$ must be a multiple of $2a_c$. Consequently, the value $2a_c$ which is as close as possible to the value $2(a_c)_{\text{ideal}}$ and which is an exact multiple of $X(e_0)$ must be found. It is given by

$$a_c = \frac{1}{2}\frac{X(e_0)}{N} \qquad (49)$$

where N is the total number of fundamental strips having their axial dimension as close as possible to the ideal axial dimension $2(a_c)_{\text{ideal}}$ that is consistent with the quantity $X(e_0)$. It is given by

$$N = \text{Round}\left(\frac{X(e_0)}{2(a_c)_{\text{ideal}}}\right) = \left\lceil \frac{n_c X(e_0)}{2L_c} - \frac{1}{2} \right\rceil \qquad (50)$$

Finally, the adjusted length can be found by

$$L(e_0, n_c) = n_c a_c = \frac{1}{2}\frac{n_c X(e_0)}{\left\lceil \frac{n_c X(e_0)}{2L_c} - \frac{1}{2} \right\rceil} \qquad (51)$$

Substituting (47) in (51) and performing the needed calculations, it can be observed that the length adjustment needed to guarantee geometric compatibility is quite moderate for all eccentricity values. The latter statement is proven in Fig. 9, where the length $L(e_0, n_c)$ normalized by the desired length L_c is plotted vs the assigned eccentricity e_0 for $n_c = 30$. As seen, the magnitude of the adjustment is about $\pm 1\%$.

In Sec. VII by (43–45) the improvement in the axial stress σ, the axial stress resultant N, and the axial load P, respectively, obtained by tailoring the helical rib angle with the circumferential position has been estimated by assuming that the rib density δ of (9) is not changed by the assignment of the eccentricity e_0 to the original circular cylinder. This assumption is correct as long as only the homogenized model is being discussed. Conversely, when the actual grid is taken into consideration, as it is stated by (49) and (50), the rib spacing a_c becomes a function of the assigned eccentricity e_0 and the number of circumferential ribs n_c. Consequently the results obtained in (43–45) need to be modified slightly. More precisely, (43–45) need to be premultiplied by a correction factor $K(e_0, n_c)$ given by

$$K(e_0, n_c) = \frac{\delta_{\text{VGE}}}{\delta_{\text{IGC}}} = \frac{\frac{d_c}{(a_c)_{\text{VGE}}}}{\frac{d_c}{(a_c)_{\text{IGC}}}} = \frac{(a_c)_{\text{IGC}}}{(a_c)_{\text{VGE}}} = \frac{\frac{L(0,n_c)}{n_c}}{\frac{L(e_0,n_c)}{n_c}} = \frac{L(0, n_c)}{L(e_0, n_c)} \qquad (52)$$

Equation (52) states that the correction factor $K(e_0, n_c)$ is equal to the ratio between the length of the original circular cylinder and the length of the actual elliptical cylinder. According with Fig. 9, this ratio is quite close to the unity for each eccentricity. Therefore, it can be stated that (43–45) can be used to estimate the improvement in the axial stress σ, the axial stress resultant N, and the axial load P, respectively, obtained by tailoring the helical rib angle with the circumferential position even in the case of the actual grid. The result obtained is not exact, but it gives a good estimation.

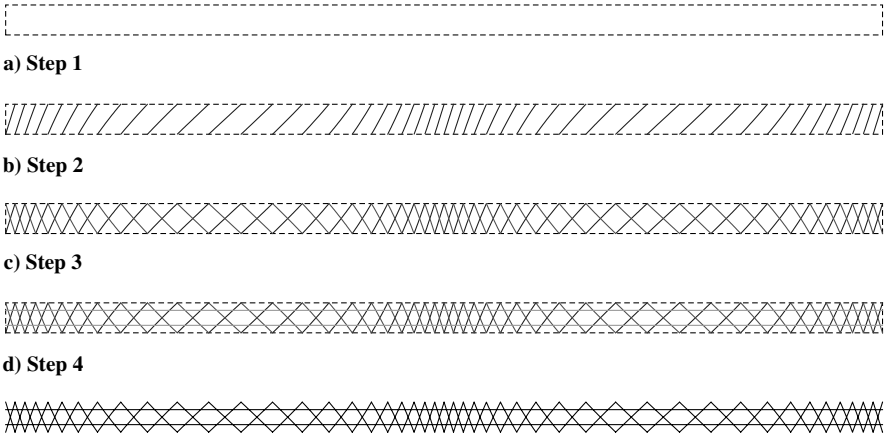

Fig. 10 Constructive procedure to build a fundamental strip $e_0 = 0.85$, $n_c = 30$.

B. Construction of the Grid

For the grid structure shown in Fig. 1, the entire grid can be constructed by attaching $n_c/2$ (since for grid continuity at the cylinder ends and for practical purposes n_c is taken to be even, so $n_c/2$ is always an integer) fundamental strips of axial length $2a_c$ one to another, where a_c is the spacing between circumferential ribs defined as

$$a_c(e_0, n_c) = \frac{L(e_0, n_c)}{n_c} \tag{53}$$

The fundamental strip can be obtained with the four steps listed next and illustrated in Fig. 10 for $e_0 = 0.85$ and $n_c = 30$:

1) Consider a fundamental strip of circumferential dimension $2\pi R_c$ and axial dimension $2a_c$ as shown in Fig. 10a, where the circumferential dimension is horizontal.

2) Consider the one helical rib in Fig. 8 that extends the entire length of the cylinder and which has one end attached to the lower left corner of the fundamental strip. Apply the cut and shift procedure to this helical rib as follows: Start at the lower end of the rib. Move up and to the right along the rib until traveling an axial distance of $2a_c$. Cut the rib. Move up and to the right until traveling an addition axial distance $2a_c$. Make another cut in the rib and then shift the cut short section of rib downward. Continue this procedure until reaching the end of the rib. The fundamental strip at this point will appear as in Fig. 10b.

3) Consider a second helical rib that extends the entire length of the cylinder and that has one end attached to the lower right corner of the fundamental strip. Apply the cut and shift procedure to this rib as with the first rib: Start at the lower end of the rib. Move up and to the left along the rib until traveling an axial distance of $2a_c$. Cut the rib. Move up and to the left until traveling a addition axial distance $2a_c$. Make another cut in the rib and then shift this short cut section of rib downward. Continue this procedure until reaching the end of the rib. The fundamental strip at this point will appear as in Fig. 10c.

4) Add two circumferential ribs (i.e., two horizontal lines) having axial position $a_c/2$ and $3a_c/2$, respectively, as shown in Fig. 10d. This completes the fundamental strip, as illustrated in Fig. 10e.

Looking at Fig. 10e it is seen that a fundamental strip contains two entire circumferential ribs and two entire helical ribs. The latter statement is true because, due to the adjustment of the cylinder length (51), the cut and shift procedure applied to a strip having axial dimension $2a_c$ results in the maximum axial position of the last section of helical rib to be exactly $2a_c$. The entire grid can be obtained by adding $n_c/2$ fundamental strips, one adjacent to another. The grids obtained for $e_0 = 0$, $e_0 = 0.50$, $e_0 = 0.70$, and $e_0 = 0.85$ are shown in Figs. 11–14, respectively. As seen from these figures, the variable geometry of the grid becomes more evident as the eccentricity increases. The variable geometry produces an increased density of the helical ribs in the more curved regions of the elliptical cross section ($t = 0$, π). The distance between the helical ribs becomes narrower as the eccentricity increases. Conversely, the density of the helical ribs is decreased in the flatter regions of the cross section ($t = \pi/2, 3\pi/2$) and the distance between helical ribs becomes wider as the eccentricity increases. This variable geometry leads to a circumferentially uniform critical strain level, but the axial modulus of the cylinder is modulated so as to produce a higher stress level in the more curved regions.

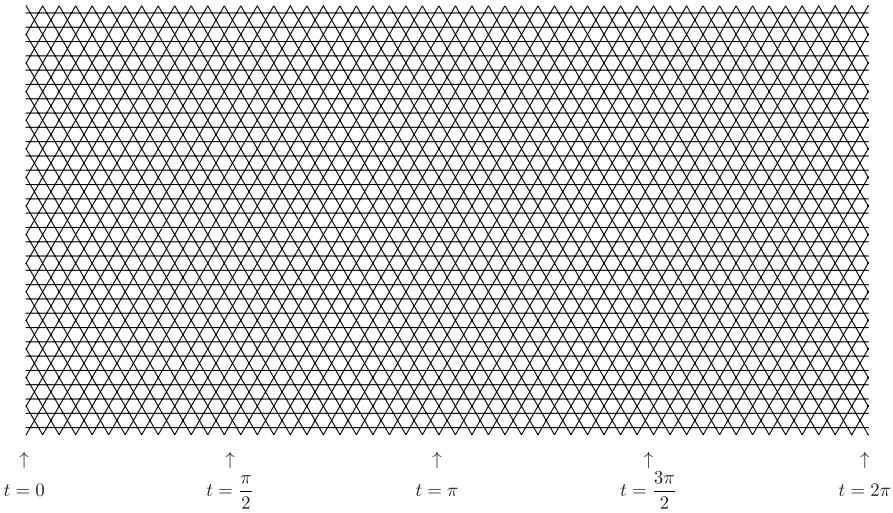

Fig. 11 Unrolled VGE cylinder, $e_0 = 0.00$, variable ϕ.

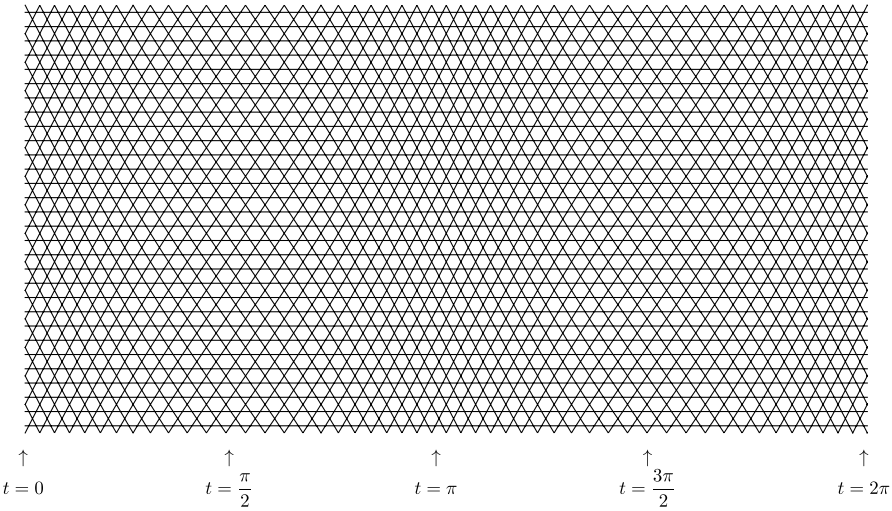

Fig. 12 Unrolled VGE cylinder, $e_0 = 0.50$, variable ϕ.

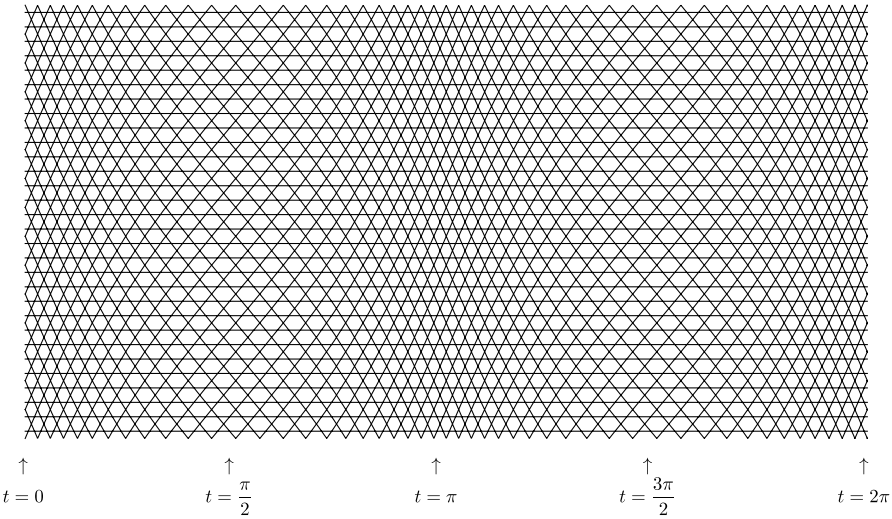

Fig. 13 Unrolled VGE cylinder, $e_0 = 0.70$, variable ϕ.

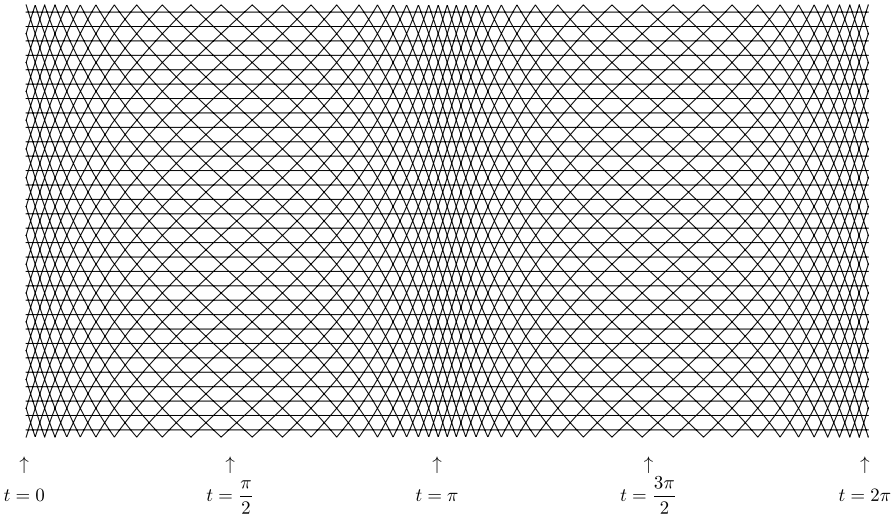

Fig. 14 Unrolled VGE cylinder, $e_0 = 0.85$, variable ϕ.

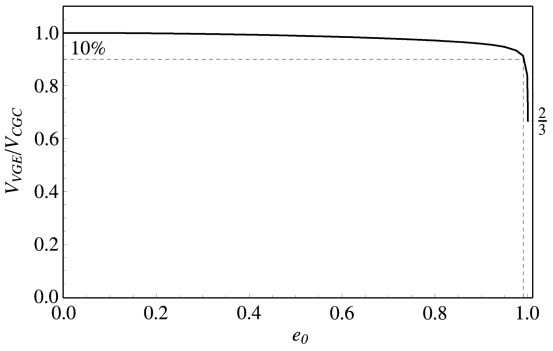

Fig. 15 Ratio $V_{\mathrm{VGE}}/V_{\mathrm{IGC}}$ vs assigned eccentricity.

C. Cylinder Volume

The volume of the lattice construction can be estimated multiplying the total length of the ribs in the cylinder by the cross-sectional area of one rib. It can be easily realized that for an assigned eccentricity of e_0 all the helical ribs have equal length l_h. Moreover, the length of circumferential ribs l_c is independent of the eccentricity and is equal to the cylinder circumference, namely $2\pi R_c$. Consequently, considering n_h to be the total number of helical ribs ($n_h/2$ at $+\phi$ and $n_h/2$ at $-\phi$) and n_c the total number of circumferential ribs, the total length l_{total} of all the ribs is

$$l_{\mathrm{total}} = n_h l_h + n_c l_c \tag{54}$$

Because of the constraint Eq. (8) that produces the grid structure shown in Fig. 1, the total number of helical ribs must be equal to the total number of circumferential ribs, i.e., $n_h = n_c$. Using (46), the infinitesimal length of each helical rib can be written as

$$\mathrm{d}\, l_h = \sqrt{1 + \left(\frac{\partial x(s, e_0)}{\partial s}\right)^2}\,\mathrm{d}s = \frac{\mathrm{d}s}{\sin(\phi(s, e_0))} \tag{55}$$

The total length of each helical rib can be obtained integrating (55) around the circumference as

$$l_h = \int_0^{2\pi R_c} \frac{\mathrm{d}s}{\sin(\phi(s, e_0))} \tag{56}$$

Keeping in mind that $n_c = n_h$, the ratio between the volume of the VGE cylinder and the volume of the IGC cylinder can be estimated using (54) as

$$\frac{V_{\mathrm{VGE}}}{V_{\mathrm{IGC}}} = \frac{l_c + (l_h)_{\mathrm{VGE}}}{l_c + (l_h)_{\mathrm{IGC}}} = \frac{2\pi R_c + \int_0^{2\pi R_c} \frac{\mathrm{d}s}{\sin(\phi(s,e_0))}}{2\pi R_c + \int_0^{2\pi R_c} \frac{\mathrm{d}s}{\sin(\pi/6)}}$$
$$= \frac{1}{3}\left(1 + \frac{1}{2\pi R_c}\int_0^{2\pi R_c} \frac{\mathrm{d}s}{\sin(\phi(s, e_0))}\right) \tag{57}$$

Equation (57) is plotted in Fig. 15. Looking at Fig. 15 it is seen that the volume of the VGE cylinder is less than the volume of the IGC cylinder for all values of eccentricity. For practical values of eccentricity, the volume is about 5% less, an interesting finding. When the assigned eccentricity approaches unity, the ratio (57) approaches 2/3. This behavior can be understood by realizing that in the IGC cylinder each helical rib is two times longer than a circumferential rib, while in the VGE cylinder with $e_0 = 1$ the helical ribs becomes horizontal and coincident in length with circumferential ribs. Consequently, when the assigned eccentricity is varied from zero to unity, one-third of the total length is lost.

The previous arguments highlight that the tailoring of the rib angle with circumferential location based on (33) does not produce significative chances in the volume of the material in the cylinder. Moreover, these slight changes are always negative. Of course, considering a lattice construction made of homogeneous material, (57) also gives an estimation of the weight ratio between the IGC and the VGE cylinders.

Table 1 Geometrical and material properties used in the finite element calculations

Dimensions	R_c	L_c	h_c	δ	E_r
Small	0.1 m	0.32 m	1.12 mm	0.1	130 GPa
Large	0.5 m	1.60 m	2.24 mm	——	——

IX. Numerical Validation of the Proposed Design

In this section the developed VGE cylinder design will be further studied using numerical results computed with the general-purpose finite element code ABAQUS [25]. The finite element model is based on the four-node SR4 element from the ABAQUS library. Each element uses the homogenized material properties which reflect the rib angle at the circumferential location of the centroid of the element, i.e., rib angle vs circumferential locations from Fig. 6. The model employs 168 equispaced nodes in the circumferential direction and 81 in the axial direction, for a total of 13,440 elements. Convergence studies have shown that this mesh density is efficient and is of sufficient accuracy for the work here. The results from ABAQUS will be compared with the results from the developed analysis. Since the developed analysis was based on a rather simple premise, i.e., (1), which did not consider prebuckling rotations or stresses other than the axial stress, such comparisons will be informative. Geometrically nonlinear prebuckling analysis will be employed, and the results for S1 simple support boundary conditions will be considered. The buckling condition will be identified by applying to one end of each cylinder the smallest axial compressive displacement that causes the tangent stiffness matrix of the numerical analysis to become singular. The stress state for this condition, in particular, the axial stress level, will be considered the critical stress. To check the generality of the findings, the quantities of interest at the critical level will be compared with the respective analytical predictions for three values of assigned eccentricity ($e_0 = 0.50, 0.70, 0.85$) and for two cylinder sizes, which are based on so-called large and small circular cylinders as described in Table 1.

In addition to using ABAQUS to compute results for VGE cylinders for three values of eccentricity and two cylinder sizes, for each cylinder size and each value of eccentricity ABAQUS is also used to compute results for the IGE cylinder. Comparison between the IGE and the IGC cylinders will be a measure of the reduction of buckling capacity of the elliptical cross section compared with the circular cross section for isogrid construction, as predicted in Fig. 3.

In Fig. 16 the circumferential variation of the axial stress at the buckling condition from the finite element results for the VGE cylinders and IGE cylinders are shown. In each subfigure the axial stresses, normalized by the buckling stress of a IGC cylinder, as a function of normalized circumferential location, are plotted. Since the material is homogeneous through the thickness, which is uniform with circumferential location, the axial stress ratio is also the axial stress resultant ratio. The analytical prediction (43) and (44) for the ratio $\sigma_{\mathrm{VGE}}/\sigma_{\mathrm{IGC}}$ ($N_{\mathrm{VGE}}/N_{\mathrm{IGC}}$) is also illustrated in the figures. For the purpose of discussion, the axial stress (axial stress resultant) for the IGC cylinder, σ_{IGC} (N_{IGC}), is included and is the horizontal line at unity. At first glance it is clear from Fig. 16 that, importantly, the prediction by the developed analysis of the σ (N) vs s relation is very close to the finite element calculations for all cases. Looking at more detail, it is observed that while the axial stress (axial stress resultant) for the IGE cylinder, σ_{IGE} (N_{IGE}), is nearly uniform around the circumference, and always less than that of the IGC cylinder, the axial stress (axial stress resultant) for the VGE cylinder, σ_{VGE} (N_{VGE}), has considerable amplitude modulation, being largest in the more curved regions of the elliptical cross section in all cases ($s/2\pi R_c = 0,\ 0.5$). This follows because the amplitude of σ (N) should be proportional to the axial modulus and, recall in the discussion related to Fig. 6, that the axial modulus in the more highly curved regions, where $\phi < \pi/6$, is higher than the axial modulus in the flatter regions, where $\phi > \pi/6$. That stiffness attracts loads and softness sheds loads is reflected in this modulated behavior of the

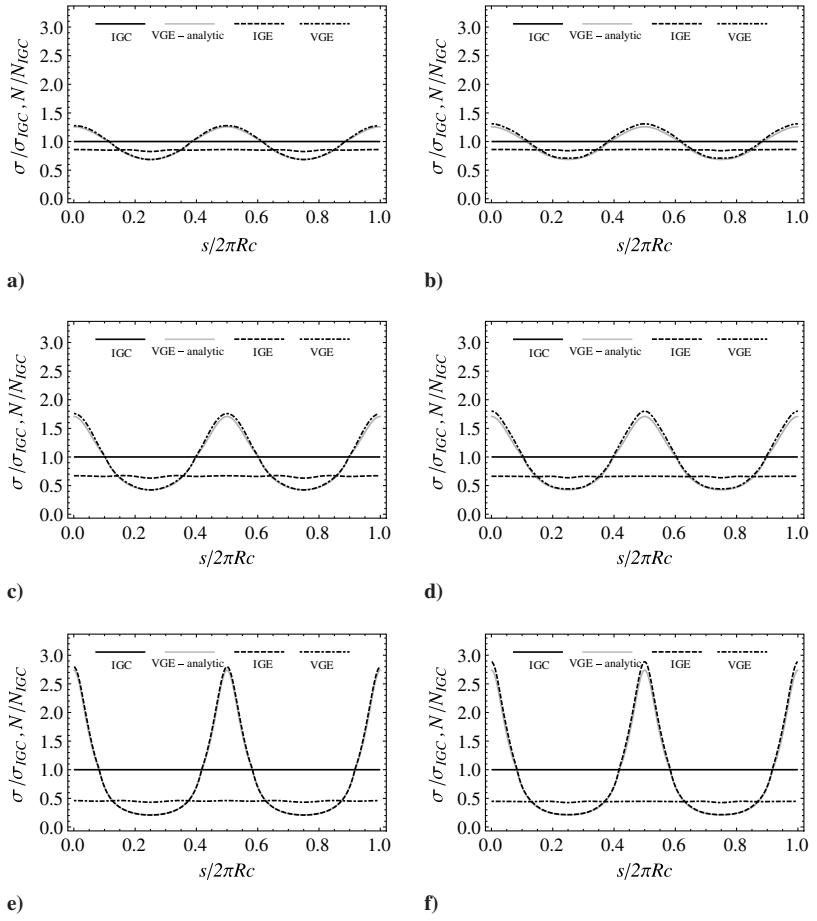

Fig. 16 Comparison among the axial stresses and axial stress resultants at the buckling condition for small and large VGE and IGE cylinders for different eccentricities: a) $e_0 = 0.50$ small, b) $e_0 = 0.50$ large, c) $e_0 = 0.70$ small, d) $e_0 = 0.70$ large, e) $e_0 = 0.85$ small, and f) $e_0 = 0.85$ large.

axial stress (axial stress resultant). It should be noted that σ_{VGE} (N_{VGE}) intersects σ_{IGC} (N_{IGC}) where the radius of curvature of the ellipse is equal to the radius of original circle, R_c [see (40) and related discussion]. The area under the relationship for N vs s is the total axial load. From a qualitative inspection of Fig. 16 it is quite evident that for each case the area under the N_{IGE} relation is less than the area under the other two, reaffirming the fact that the axial buckling capacity of the IGE cylinder is less than that of the IGC cylinder, and, more important, that tailoring of the rib angle with circumferential location results in an increase of the axial buckling capability of a VGE cylinder with respect to a IGE cylinder. Moreover, it can be noted that the developed analysis given by (45) seems to predict the stresses very well in the over-shear GMI regions, whereas in the undershear GMI regions the developed analysis seems to slightly underpredict the stresses.

A quantitative comparison among key buckling load ratios of the VGE, IGE, and IGC cylinders at the buckling condition, as computed from finite element analyses and as predicted by the developed analysis, is given in Table 2. Looking at Table 2, a few comments can be made. First, as mentioned, the ratio $P_{\mathrm{IGE}}/P_{\mathrm{IGC}}$ is a measure of the reduction in axial buckling load capacity of the isogrid elliptical cylinder relative to the baseline IGC cylinder. As seen from columns two through four in the table, the prediction given by (25), and in Fig. 3, from the developed analysis is within 10% of the finite element calculations. Second, the ratio $P_{\mathrm{VGE}}/P_{\mathrm{IGC}}$ is a measure of the restoration of the axial buckling load, by way of rib angle tailoring, of the elliptical cylinder relative to the baseline IGC cylinder. As observed from columns five through seven, the prediction given by (45), and in Fig. 7, only slightly underestimates the level of restoration, the underestimation being 5%, at most. Finally, the ratio $P_{\mathrm{VGE}}/P_{\mathrm{IGE}}$ is a measure of the gain through rib angle tailoring of the axial buckling load of an elliptical cylinder. It can be observed from the last two columns that even if rib angle tailoring is unable to completely restore the axial buckling load of an elliptical cylinder to the axial buckling load of the baseline IGC cylinder, tailoring of the rib angle for the elliptical cylinder results in a relevant increase in the buckling performance. The increase is dependent on the assigned eccentricity. More precisely, the finite element analyses predict the axial load increase to vary from about 15% for $e_0 = 0.50$ to about 100% for $e_0 = 0.85$. Moreover, based on Fig. 15, it can be seen that the load increase is accompanied by a decrease of the weight of the lattice cylinder.

Table 2 Comparison among key load ratios of VGE, IGE, and IGC cylinders at the buckling condition

	$P_{\mathrm{IGE}}/P_{\mathrm{IGC}}$			$P_{\mathrm{VGE}}/P_{\mathrm{IGC}}$			$P_{\mathrm{VGE}}/P_{\mathrm{IGE}}$	
	Numerical			Numerical			Numerical	
e_0	Small	Large	Analytical [Eq. (25)]	Small	Large	Analytical [Eq. (45)]	Small	Large
0.50	0.8508	0.8559	0.8090	0.9702	0.9900	0.9582	1.1403	1.1562
0.70	0.6626	0.6583	0.6163	0.9459	0.9599	0.9185	1.4275	1.4583
0.85	0.4526	0.4435	0.4118	0.8934	0.9154	0.8751	1.9738	2.0638

a) b) c)

Fig. 17 Deformed prebuckling shape of an axially loaded simply supported small VGE cylinder: a) $e_0 = 0.50$, b) $e_0 = 0.70$, and c) $e_0 = 0.85$.

The deformed shapes of simply supported axially loaded small VGE elliptical cylinders just before buckling as computed by the finite element analysis for the three levels of eccentricity are illustrated in Fig. 17. As seen, although the majority of the deformations are confined to the boundary layers at the ends of the cylinder, the deformations are distributed around the circumference. This can be realized by comparing Fig. 17b which represents the VGE cylinder with eccentricity 0.70, with Fig. 4b, which represents the IGE cylinder with the same value of eccentricity.

X. Conclusions

In a general sense, the results presented have illustrated the gains that can be achieved by considering structures that use continuously varying material properties to mitigate a structural feature which is detrimental to load capacity or some other measure of performance. In the specific case here, the material properties of an elliptical lattice cylinder were continuously varied by varying rib angle to prevent there from being any particular circumferential location around the cylinder that was more susceptible to axial buckling than any other circumferential location. Additionally, the elliptical cylinder was designed to have the same level of buckling strain as a baseline IGC cylinder of the same circumference. The designed variable rib angle orthogrid cylinder resulted in regaining much of the buckling load that was lost when the circular isogrid cylinder was made elliptical, and with no increase in weight. As shown, these predictions were made with considerable accuracy with the developed analysis when compared with a more refined analysis based on finite elements. The good comparison is particularly interesting given that the developed analysis was based on a single simple equation, namely, (1). Also, that simple equation in the form of (27) illustrates a broader view of tailoring, beyond elliptical cylinders, and beyond orthogrid construction. Specifically, for a particular noncircular cross section $\rho(t, e_0)$ in (27) is a known function, where now e_0 is some measure of the deviation of the cross section from being circular. The other terms on the right-hand side of (27), $\varphi(t, e_0)$ and $E_1(t, e_0)$, are material properties and provide some flexibility for using tailoring to achieve a specific result on the left hand side. These two functions can be varied somewhat independently with circumferential location in a specific fashion to achieve a desired result ("somewhat" because there are physical limits to how much material properties can be varied). Equation (27) provides an opportunity to expand thinking about material tailoring.

Before closing it is important to note that the issues of material failure and postbuckling performance have not been addressed here. The latter subject is beyond the scope of the present paper, particularly as the postbuckling deformation patterns could be such that local modeling of the orthogrid ribs, including their intersections, would be necessary. Though the inward and outward postbuckling deformation pattern of cylinders can often be of a nature that they can be considered global, the importance of a local level of modeling in a postbuckled deformation state should not be ruled out without further investigation. Regarding failure up to the buckling condition: from (35), for the case of $\eta_c = 1/200$, for example, the axial bucking strain in the baseline IGC cylinder would be about 3000 $\mu\epsilon$, which would be the axial strain in an axially aligned rib, of which there are none in either the baseline IGC cylinder or the VGE cylinder. In the more highly curved regions of an elliptical cross section with an eccentricity of $e_0 = 0.85$ there are some ribs close to being axially aligned (see Fig. 14). However, 3000 $\mu\epsilon$ is not a particularly high compressive strain level for most materials, so material compressive failure would not be an issue. Regarding failure of the ribs by local (Euler) buckling up to that strain level, it can be assumed that each rib is fixed at its ends [3] and the maximum rib length relative to the smallest radius of gyration of the rib cross section that can be tolerated can be determined for cylinders applied to specific situations. Finally, it should be noted that it is expected that if the variable rib angle cylinder designs developed here were applied to cylinders with clamped boundaries, similar gains in performance would be observed. This was the case in Sun and Hyer [18] where designs for fiber angle variations with circumferential location based on analyses using simple support conditions were applied to cylinders with clamped supports. Also, Paschero and Hyer [15] found this to be the case for variable wall thickness designs.

References

[1] *Isogrid Design Handbook*, NASA CR 124075, 1973, Revision A.

[2] Noor, A., "Continuum Modeling of Repetitive Lattice Structures," *Applied Mechanics Reviews*, Vol. 41, No. 7, 1988, pp. 285–296. doi:10.1115/1.3151907

[3] Chen, H., and Tsai, S., "Analysis and Optimum Design of Composite Grid Structures," *Journal of Composite Materials*, Vol. 30, No. 4, 1996, pp. 503–534.

[4] Hohe, J., and Becker, W., "Effective Elastic Properties of Triangular Grid Structures," *Composite Structures*, Vol. 45, No. 2, 1999, pp. 131–145. doi:10.1016/S0263-8223(99)00016-1

[5] Hohe, J., Beschorner, C., and Becker, W., "Effective Elastic Properties of Hexagonal and Quadrilateral Grid Structures," *Composite Structures*, Vol. 46, No. 1, 1999, pp. 73–89. doi:10.1016/S0263-8223(99)00048-3

[6] Kim, T. D., "Fabrication and Testing of Composite Isogrid Stiffened Cylinder," *Composite Structures*, Vol. 45, No. 1, 1999, pp. 1–6. doi:10.1016/S0263-8223(98)00124-X

[7] Vasiliev, V. V., Barynin, V. A., and Rasin, A. F., "Anisogrid Lattice Structures: Survey of Development and Applications," *Composite Structures*, Vol. 54, Nos. 2–3, 2001, pp. 361–370. doi:10.1016/S0263-8223(01)00111-8

[8] Huybrechts, S. M., Meink, T. E., Wegner, P. M., and Ganley, J. M., "Manufacturing Theory for Advanced Grid Stiffened Structures," *Composites Part A*, Vol. 33, No. 2, 2002, pp. 155–166. doi:10.1016/S1359-835X(01)00113-0

[9] Hualin, F., and Wei, Y., "An Equivalent Continuum Method of Lattice Structures," *Acta Mechanica Solida Sinica*, Vol. 19, No. 2, 2006, pp. 103–113. doi:10.1007/s10338-006-0612-x

[10] Li, G., and Chen, J., "A Generalized Analytical Modeling of Grid Stiffened Composite Structures," *Journal of Composite Materials*, Vol. 41, No. 24, 2007, pp. 2939–2969. doi:10.1177/0021998307082180

[11] Fan, H. L., Meng, F. H., and Yang, W., "Sandwich Panels with Kagome Lattice Cores Reinforced by Carbon Fibers," *Composite Structures*, Vol. 81, No. 4, 2007, pp. 533–539. doi:10.1016/j.compstruct.2006.09.011

[12] Fan, H., Fang, D., and Jin, F., "Mechanical Properties of Lattice Grid Composites," *Acta Mechanica Sinica*, Vol. 24, No. 4, 2008, pp. 409–418.

doi:10.1007/s10409-008-0162-1
[13] Fan, H., Fang, D., and Jin, F., "Mechanical Properties of Lattice Grid Composites" (Errata), *Acta Mechanica Sinica*, Vol. 24, No. 5, 2008, p. 591.
doi:10.1007/s10409-008-0195-5
[14] Fan, H., and Fang, D., "Anisotropic Mechanical Properties of Lattice Composite Grids," *Journal of Composite Materials*, Vol. 42, No. 23, 2008, pp. 2445–2460.
doi:10.1177/0021998308095888
[15] Paschero, M., and Hyer, M. W., "Improvement of Axial Load Capacity of Elliptical Cylindrical Shells," *AIAA Journal*, Vol. 47, No. 1, Jan. 2009, pp. 142–156.
doi:10.2514/1.37012
[16] Blom, A., Stickler, P., and Gürdal, Z., "Optimization of a Composite Cylinder Under Bending by Tailoring Stiffness Properties in Circumferential Direction," *Composites Part B*, Vol. 41, No. 2, 2010, pp. 157–165.
doi:10.1016/j.compositesb.2009.10.004
[17] Blom, A., Setoodeh, S., Hol, J., and Gürdal, Z., "Design of Variable-Stiffness Conical Shells for Maximum Fundamental Frequency," *Computers and Structures*, Vol. 86, No. 9, 2008, pp. 870–878.
doi:10.1016/j.compstruc.2007.04.020
[18] Sun, M., and Hyer, M. W., "Use of Material Tailoring to Improve Buckling Capacity of Elliptical Composite Cylinders," *AIAA Journal*, Vol. 46, No. 3, 2008, pp. 770–782.
doi:10.2514/1.32495
[19] Paschero, M., and Hyer, M. W., "Axial Buckling of an Orthotropic Circular Cylinder: Application to Orthogrid Concept," *International Journal of Solids and Structures*, Vol. 46, No. 10, 2009, pp. 2152–2171.
doi:10.1016/j.ijsolstr.2008.08.033
[20] Brush, D., and Almroth, B., *Buckling of Bars, Plates, and Shells*, McGraw–Hill, New York, 1975, p. 168.
[21] Jones, R., *Buckling of Bars, Plates, and Shells*, Bull Ridge, Blacksburg, VA, 2006, chap. 4.
[22] Kempner, J., and Chen, Y. N., "Buckling and Postbuckling of an Axially Compressed Oval Cylindrical Shell," *Proceedings: Symposium on Theory of Shells to Honor Lloyd Hamilton Donnell*, edited by D. Muster and U. Houston, McCutchan, 1967, pp. 141–175.
[23] Vasiliev, V. V., *Mechanics of Composite Structures*, Taylor and Francis, Washington, D.C., 1993.
[24] Y. Miyamoto, W. Kaysser, B. Rabin, A. Kawasaki, and R. Ford (eds.), *Functionally Graded Materials: Design, Processing and Applications*, Kluwer Academic, Boston, 1999.
[25] ABAQUS, Ver. 6.6, Dassault Systèmes Simulia, Providence, RI, 2006, www.abaqus.com.

A. Palazotto
Associate Editor